Single-molecule magnet Mn_{12} on GaAs-supported graphene: Gate field effects from first principles

Shuanglong Liu,[1,2,3] Maher Yazback,[1,2,3] James N. Fry,[1] Xiao-Guang Zhang,[1,2,3] and Hai-Ping Cheng[1,2,3,*]

[1]*Department of Physics, University of Florida, Gainesville, Florida 32611, USA*

[2]*Quantum Theory Project, University of Florida, Gainesville, Florida 32611, USA*

[3]*Center for Molecular Magnetic Quantum Materials, University of Florida, Gainesville, Florida 32611, USA*

(Received 8 December 2020; accepted 20 December 2021; published 3 January 2022)

We study gate field effects on the heterostructure $Mn_{12}O_{12}(COOH)_{16}(H_2O)_4$|graphene|GaAs via first-principles calculations. We find that under moderate doping levels, electrons can be added to but not taken from the single-molecule magnet $Mn_{12}O_{12}(COOH)_{16}(H_2O)_4$ (Mn_{12}). The magnetic anisotropy energy (MAE) of Mn_{12} decreases as the electron-doping level increases due to electron transfer from graphene to Mn_{12} and change in the band alignment between Mn_{12} and graphene. At an electron-doping level of $-5.00 \times 10^{13}\,\mathrm{cm}^{-2}$, the MAE decreases by about 18% compared with zero doping. The band alignment between graphene and GaAs is more sensitive to electron doping than to hole doping, since the valence band of GaAs is close to the Fermi level. The GaAs substrate induces a small band gap in the supported graphene under zero gate field and a nearly strain-free configuration. Finally, we propose a vertical tunnel junction for probing the gate dependence of MAE via electron transport measurements.

DOI: 10.1103/PhysRevB.105.035401

I. INTRODUCTION

$Mn_{12}O_{12}(COOR)_{16}(H_2O)_4$, where R represents $-CH_3$ or other ligands, is a prototypical single-molecule magnet (SMM) [1] whose magnetic and electronic properties have been studied since the late '90s [2–6]. This molecule is also interesting as a spin system because its total magnetic moment puts it near the boundary between classical and quantum regimes. Tunneling magnetism measurements show its quantum nature [7], but its big magnetic moment ($S = 10$) makes it almost classical. The magnetic anisotropy energy (MAE) of $Mn_{12}O_{12}(COOR)_{16}(H_2O)_4$, which forms the barrier for magnetic tunneling, depends on the type of ligand [8–32] as well as the charge state of the molecule. In experiments, one- or two-electron reduced $Mn_{12}O_{12}(COOR)_{16}(H_2O)_4$ has been synthesized by adding PPh_4^+ or other cations to the molecular crystal [13,33–37]. The resulting negatively charged $Mn_{12}O_{12}(COOR)_{16}(H_2O)_4$ with an integer number of electrons yields a decreased MAE for $-CHCl_2$ [35] or $-C_6F_5$ [13] ligands. Based on computations, a decreased MAE has also been reported for negatively charged $Mn_{12}O_{12}(COOR)_{16}(H_2O)_4$ with $-H$ [6] or $-C_6H_5$ [38] ligands. When a magnetic molecule is adsorbed on a surface, a fractional number of electrons may be transferred to/from the molecule, modifying its MAE [39–42].

Most earlier experiments were performed either in solution or in molecular crystals. Recently, Hebard's [43] group experimentally investigated the gate-voltage dependence of transport properties of $Mn_{12}O_{12}(COOR)_{16}(H_2O)_4$ on graphene surfaces (supported by Si) with different ligands. The applied gate voltage is believed to affect transport properties by modulating the charge transfer between graphene and $Mn_{12}O_{12}(COOR)_{16}(H_2O)_4$. However, such experiments were unable to determine whether the MAE of $Mn_{12}O_{12}(COOR)_{16}(H_2O)_4$ is also tuned by the gate voltage and the charge transfer induced by it. It is also not clear how the coupling to a semiconductor substrate changes the magnetic and electronic properties of the molecule. In this paper, we aim to answer these questions through a first-principles calculation using $Mn_{12}O_{12}(COOH)_{16}(H_2O)_4$ (Mn_{12}) as an example.

We choose GaAs-supported graphene (Gr|GaAs) as substrate. Compared to a Si substrate, GaAs provides free carriers at lower temperatures [44,45]. This allows transport measurements at lower temperatures, where the magnetic properties of SMMs are better observed. Common stable GaAs surfaces include (100) [46,47] and (111) [48,49] with various surface reconstructions. The GaAs (111) surface has the closest lattice match with the graphene lattice. Munshi *et al.* reported the growth of GaAs nanorods on few-layer graphene, where a GaAs(111) surface is in contact with the top graphene layer [50]. Several epitaxial atomic structures of the interface between GaAs(111) and graphene have been proposed in literature bt all with relatively large strain in graphene [50,51]. Here, we propose a different atomic structure where the strain in graphene is close to zero. Using this structure, we simulate gate-field effects on the Gr|GaAs interface with and without the adsorption of Mn_{12}. For brevity, we denote the heterostructure with Mn_{12} by Mn_{12}|Gr|GaAs.

The rest of the paper is organized as follows. We describe the computational details in Sec. II. We present the atomic structure, the electronic structure, and the magnetic anisotropy of the Mn_{12}|Gr|GaAs heterostructure in Secs. III A–III C. In Sec. III D, we propose a vertical tunnel junction based on

*Email address: hping@ufl.edu

TABLE I. Mulliken charge analysis for Mn_{12}|Gr|GaAs at different charge-doping levels. Each entry represents the amount of excess charge per atom. Positive (negative) values indicate gain (loss) of electrons relative to the case of zero doping. The number of atoms for Mn_{12}, graphene, the first Ga layer, and the first As layer are 100, 338, 48, and 64, respectively.

Doping level ($\times 10^{13}$ cm^{-2})	Mn_{12} ($\times 10^{-3}$)	Graphene ($\times 10^{-3}$)	First Ga layer ($\times 10^{-3}$)	First As layer ($\times 10^{-3}$)	Second Ga layer ($\times 10^{-3}$)	Second As layer ($\times 10^{-3}$)	Third Ga layer ($\times 10^{-3}$)	Third As layer ($\times 10^{-3}$)
−1.00	0.61	1.67	−6.36	−3.38	0.26	0.03	0.17	−0.14
−0.50	0.00	0.91	−3.15	−1.66	0.13	0.02	0.08	−0.06
−0.10	0.00	0.17	−0.59	−0.31	0.03	0.01	0.01	−0.01
−0.05	0.00	0.09	−0.30	−0.15	0.01	0.00	0.01	−0.01
0.00	0.00	0.00	0.00	0.00	0.00	0.00	0.00	0.00
0.05	0.00	−0.07	0.25	0.10	0.00	−0.01	−0.01	0.00
0.10	0.00	−0.18	0.62	0.30	−0.02	−0.01	−0.01	0.01
0.50	0.00	−0.19	0.56	0.13	−0.13	−0.20	−0.06	−0.07
1.00	0.00	−0.17	0.41	−0.03	−0.21	−0.36	−0.12	−0.20

the Mn_{12}|Gr|GaAs heterostructure. Finally, we conclude in Sec. IV.

II. METHOD

Allcalculations are based on density functional theory (DFT) [52,53] as implemented in the VIENNA AB INITIO SIMULATION PACKAGE (VASP) [54,55] and the SIESTA package [56]. We use VASP to relax atomic structures with no applied electric field and SIESTA to calculate electronic structures in the presence of a gate electric field. The atomic structure is kept at the relaxed configuration with no electric field.

In VASP calculations, we apply an energy cutoff of 500 eV for plane waves and projector augmented-wave pseudopotentials [57]. We adopt the exchange correlation energy functional proposed by Klimes *et al.*, optB86b [58], to include the van der Waals interaction between graphene and Mn_{12} (or GaAs). Given the large supercell size ($a = b \approx 3.2$ nm, $c = 5.2$ nm), only the Γ point is sampled in reciprocal space. The energy tolerance for electronic self-consistency and the force tolerance for ionic relaxation are set to 1×10^{-6} eV and 0.02 eV/Å, respectively. We use Gaussian smearing with a smearing parameter of 0.2 eV to facilitate the electronic self-consistent procedure. To eliminate interaction between periodic images in the perpendicular direction (with respect to the GaAs slab), a vacuum layer of at least 18 Å is added and electric dipole corrections (for both energy and force) are enabled. On-site Coulomb interaction (U) within the DFT + U method and spin-orbit interactions are not considered for ionic relaxations.

In SIESTA calculations, we apply double-ζ polarized (DZP) basis functions [56] for Mn and O atoms and single-ζ polarized (SZP) basis functions for C, H, Ga, and As atoms. Such a mixed basis set allows us to describe the magnetic properties (due to Mn atoms) accurately with less computational load. A SZP basis set is often not sufficiently accurate for structural relaxation, but it usually produces reasonably good electronic structure for a fixed atomic structure. The basis functions are optimized for Mn_{12}, graphene, and the GaAs slab separately. Detailed specifications of the basis functions are presented in Appendix A. Since the optB86b functional is not available in SIESTA and the atomic structure is fixed, we use the Perdew-Burke-Ernzerhof exchange correlation energy functional [59] instead. We apply norm-conserving pseudopotentials as generated by the Troullier-Martins scheme [60] and a mesh cutoff of 200 Ry for real space sampling. To accurately determine the Fermi energy, we adopt a 6×6 k-grid for sampling reciprocal space [61] and the fourth-order Methfessel-Paxton smearing method [62] with a smearing temperature of 200 K. Results of convergence tests with respect to the smearing temperature and with respect to the k grid are given in Tables III and IV, respectively, (see Appendix B). The effects of a single back gate are modeled via the effective screening medium (ESM) method [63]. In the single gate configuration, the boundary condition for the back-gate (vacuum) side is constant electrostatic potential (vanishing first derivative of the potential). Such a nonperiodic boundary condition for the electrostatic potential is imposed by the corresponding Green's function in the ESM method. In our simulations, the back-gate (vacuum) boundary is 15 Å below (above) the bottom (the top) of the system under study. To improve the numerical results for band alignment within the heterostructure Mn_{12}|Gr|GaAs, we treat the semicore Ga d electrons as valence electrons and adopt the DFT + 1/2 approach for GaAs [64,65]. A DFT + 1/2 cutoff radius of 3.8 Bohr is applied to limit the range of self-energy potential for As $4p$ orbitals [66]. The DFT + 1/2 band gap of bulk GaAs is calculated to be 1.526 eV, in good agreement with the experimental value of 1.52 eV at low temperatures [44] as opposed to 0.236 eV without this approach. For the same purpose of improving the band alignment, we apply the DFT + U method proposed by Dudarev *et al.* [67] and set the on-site Coulomb interaction U to 4 eV for Mn atoms. This value for U yields good agreement of the density of states of Mn_{12} compared with x-ray photoemission spectra and x-ray emission spectra measurements [68].

We also use the SIESTA package to calculate the MAE of Mn_{12} on graphene without the GaAs substrate (to be justified later). Spin-orbit interactions are included via the pseudopotentials [69,70] and evaluated in an on-site approximation

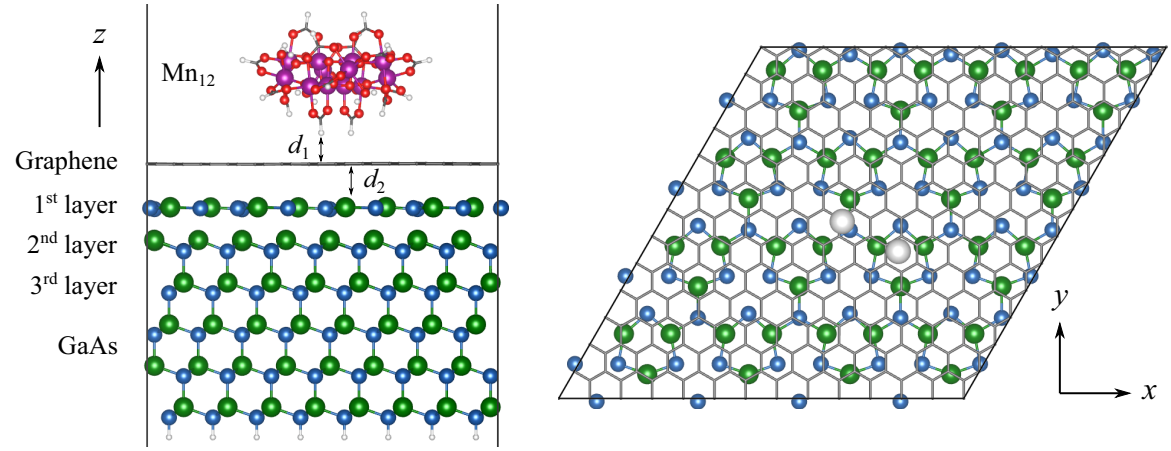

FIG. 1. Side view (left) and top view (right) of the Mn_{12}|Gr|GaAs heterostructure. In the side view, $d_1 \approx 2.46$ Å and $d_2 \approx 3.42$ Å. In the top view, only graphene and the atoms adjacent to graphene are shown. The hydrogen atoms of Mn_{12} are magnified for visibility. Purple: manganese, red: oxygen, gray: carbon, white: hydrogen, green: gallium, and blue: arsenic.

[71]. At high electron-doping levels, the self-consistent calculation fails to converge with the Methfessel-Paxton smearing method. This convergence problem is solved by using the Fermi-Dirac smearing method. To improve the numerical accuracy, we apply a 24×24 k grid together with a smearing parameter of 0.041 eV and an energy tolerance of 1×10^{-6} eV for electronic self-consistency. We set the spin-orbit coupling strength parameter to be 1.34, such that the calculated MAE (5.2 meV, or 61 K) of $Mn_{12}O_{12}(COOCH_3)_{16}(H_2O)_4$ is close to the experimental value [72]. The DFT + U method is not applied for calculating the MAE.

III. RESULTS

A. Atomic structure

Figure 1 shows the atomic structure of the heterostructure Mn_{12}|Gr|GaAs. The GaAs(111) surface is modeled by a slab consisting of six Ga atomic layers and six As atomic layers. The top two atomic layers are stabilized by a 2×2 reconstruction with Ga vacancies [49]. Each As atom at the bottom is terminated by a pseudo hydrogen atom with 0.75 electrons to avoid fictitious surface bands. The lattice constants of bulk GaAs and graphene are 5.653 and 2.461 Å, respectively. We found a good lattice match for the supercell shown in Fig. 1, which contains 4×4 GaAs unit cells (with surface reconstruction) and 13×13 graphene unit cells. This allows graphene to match the GaAs lattice with only a 0.04% compression.

During atomic relaxation, all atoms are relaxed except the bottom three Ga (As) atomic layers to mimic the bulk environment of GaAs. Without the Mn_{12} molecule, graphene already buckles slightly due to the nonuniform interaction with GaAs. The maximal out-of-plane displacement of graphene (carbon atoms) is about ± 0.08 Å, which is one order of magnitude larger than in-plane displacements. After the adsorption of Mn_{12}, graphene is further distorted, with a maximal out-of-plane displacement of about ± 0.03 Å. Due to relatively weak chemical bonds between the core of the Mn_{12} molecule and the surrounding ligands, the molecule is prone to distortion and losing parts of the ligands. For example, Mn_{12} loses its structural integrity when deposited on a Au(111) surface [73]. In contrast, previous DFT calculations suggest that Mn_{12} remains intact on graphene [4]. In the current study, the structure of Mn_{12} also remains intact with slight structural distortion when it is adsorbed on Gr|GaAs. Figures 2(a) and 2(b) show histograms of the number of chemical bond lengths and bond angles versus change in the bond length or bond angle. All bond lengths or bond angles of Mn_{12} change by no more than 0.03 Å or 4°. A fraction 69.5% of all chemical bond lengths and 60.4% of bond angles of Mn_{12} change within the range of $[-0.005 : 0.005]$ Å and $[-0.25 : 0.25]$°. However, there are eight Mn–O bonds which change by more than 0.015 Å in length. Each of these–O bonds stems from a Mn^{3+} ion of the outer Mn_8O_8 ring, and all of them point toward graphene (from Mn to O). Also, there are two Mn–O–H bond angles that change by more than 3.5°. For both of these–O–H entities, the O–H bond belongs to a H_2O unit and the Mn–O bond length changes by more than 0.015 Å.

B. Electronic structure

Now, we turn to the electronic structure of the Mn_{12}|Gr|GaAs heterostructure under both zero and finite gate electric fields. Without spin-orbit coupling, isolated graphene is a semimetal, without an energy gap at the Fermi level. When graphene is supported on the GaAs(111) surface, calculation using SIESTA shows an energy gap of 2.2 meV at the Dirac point. There are two possible factors that can induce such an energy gap in graphene: (1) a structural distortion in graphene itself and (2) the nonuniform potential due to the GaAs substrate. To identify which factor is responsible for the gap, we remove the GaAs substrate and compute the band structure for isolated graphene but with the same structural distortion. The resulting band structure is gapless to within our numerical precision (∼0.1 meV). From this, we conclude that the 2.2 meV energy gap is due to the nonuniform potential of the GaAs substrate. The band gap of graphene does not change after adsorption of Mn_{12}.

In the Mn_{12}|Gr|GaAs heterostructure, both graphene and GaAs are nonmagnetic and, according to our spin-polarized DFT calculations, both the highest occupied molecular

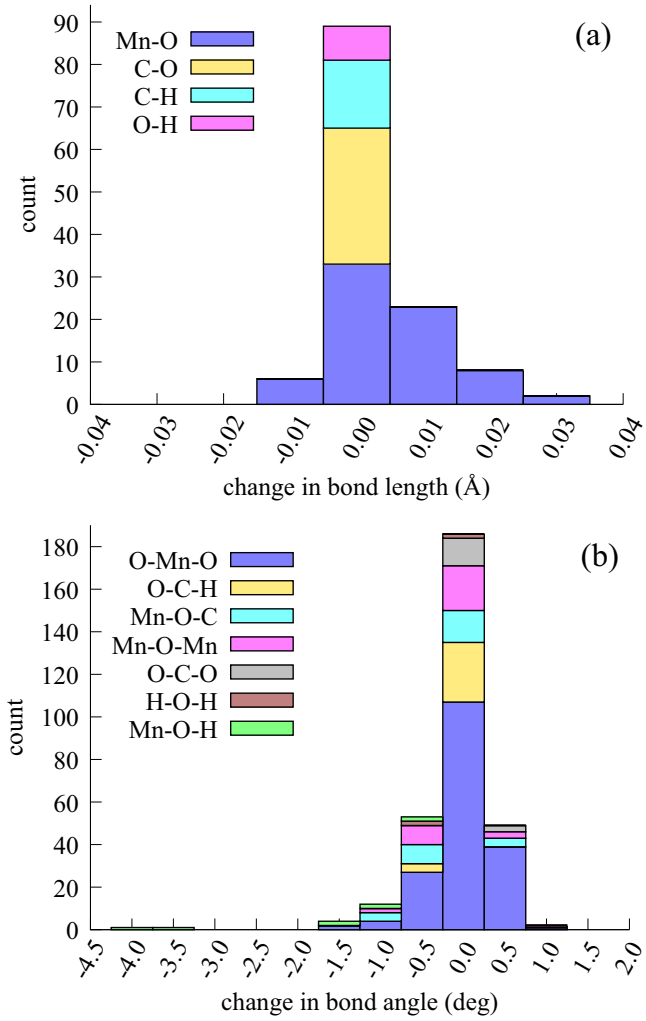

FIG. 2. Statistics of (a) bond length changes and (b) bond angle changes of Mn_{12}. The comparison is between the Mn_{12} molecule adsorbed on Gr|GaAs and an isolated free Mn_{12} molecule.

orbital (HOMO) and the lowest unoccupied molecular orbital (LUMO) of Mn_{12} have the same spin. We define this spin to be spin up. Figure 3 shows the spin-up energy bands of this heterostructure. The Fermi level lies within the 2.2 meV energy gap of graphene. Relative to the Fermi energy, the HOMO orbital of Mn_{12}, the LUMO orbital of Mn_{12}, the valence band maximum (VBM) of GaAs, and the conduction band minimum (CBM) of GaAs lie at $E_{\mathrm{HOMO}} = -0.681\,\mathrm{eV}$, $E_{\mathrm{LUMO}} = 0.192\,\mathrm{eV}$, $E_{\mathrm{VBM}} = -0.035\,\mathrm{eV}$, and $E_{\mathrm{CBM}} = 1.496\,\mathrm{eV}$. Compared with these four typical energies, the band gap of graphene is much smaller. For this reason, and for convenience of discussion, we will denote the *Dirac point* as the middle of the apexes of the upper and lower Dirac cones, even though the two cones are not quite connected. The LUMO energy E_{LUMO}, the energy of the Dirac point E_{Dirac}, and the valence band maximum E_{VBM} together dictate the band alignment between Mn_{12}, graphene, and GaAs.

Figure 4 shows how E_{LUMO}, E_{VBM}, and E_{Dirac} are affected by carrier density, i.e., the dependence of the band alignment on electrostatic doping. A negative (positive) carrier density means electron (hole) doping. All energies are measured relative to the Fermi energy, which is set at zero. Overall, all these three typical energies decrease with electron-doping and increase with hole-doping levels. E_{Dirac} in particular is more sensitive to electron doping than hole doping. For example, E_{Dirac} is $-0.195\,\mathrm{eV}$ at a charge density of $\rho = -0.50 \times 10^{13}\,\mathrm{cm}^{-2}$, but only $+0.008\,\mathrm{eV}$ at $+0.50 \times 10^{13}\,\mathrm{cm}^{-2}$. The asymmetric response of E_{Dirac} to charge doping can be understood from two aspects. First, electrons are mainly added to (taken from) graphene before the HOMO of Mn_{12} (the VBM of GaAs) is brought to the Fermi level,

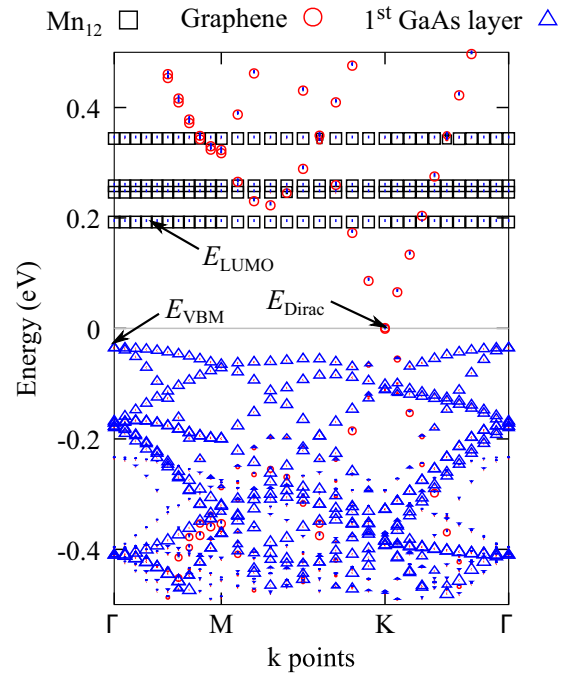

FIG. 3. Band structure of Mn_{12}|Gr|GaAs. Squares, circles, and triangles represent, respectively, Mn_{12}, graphene, and GaAs states. The size of a symbol (square, circle, triangle) is proportional to the projected density of states of the Mn_{12} molecule, graphene layer, or first GaAs layer). The Fermi level is set to zero.

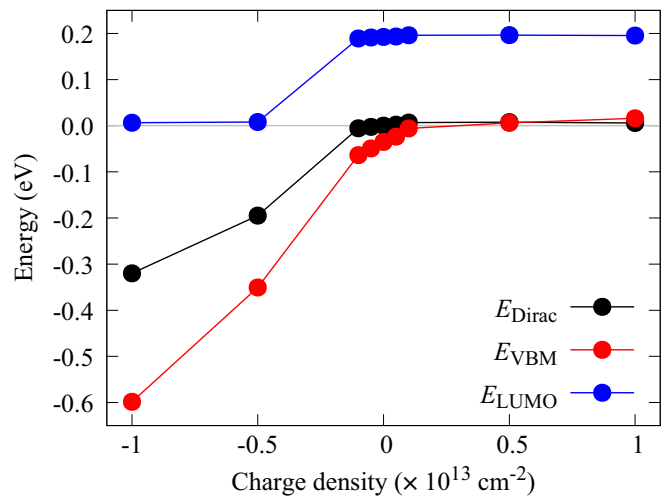

FIG. 4. The typical energies E_{LUMO}, E_{Dirac}, and E_{VBM} of Mn_{12}|Gr|GaAs versus charge-doping level.

whence Mn_{12} (GaAs) becomes charged (doped). However, the VBM of GaAs is much closer to the Fermi level than the HOMO of Mn_{12}. Second, GaAs has a much higher density of states than graphene. Therefore, the same amount of charge causes a smaller shift in the energy bands when GaAs is doped than when graphene is doped. At $\rho = -1.00 \times 10^{13}\,\mathrm{cm}^{-2}$, the LUMO orbital of Mn_{12} is only a few meV above the Fermi level. According to our calculations, the LUMO of Mn_{12} becomes partially occupied, and thus Mn_{12} is negatively charged. It is noteworthy that the Dirac point of graphene becomes lower in energy than the VBM of GaAs at a point between $\rho = 0.50 \times 10^{13}\,\mathrm{cm}^{-2}$ and $\rho = 1.00 \times 10^{13}\,\mathrm{cm}^{-2}$. We also simulate gate field effects on the band alignment of Gr|GaAs without Mn_{12}. By comparing with Mn_{12}|Gr|GaAs, we find that the influence of Mn_{12} on both E_{Dirac} and E_{VBM} is smaller than 1 meV within the charge density range of $[-0.50 : 1.00] \times 10^{13}\,\mathrm{cm}^{-2}$. At $\rho = -1.00 \times 10^{13}\,\mathrm{cm}^{-2}$, E_{Dirac} (E_{VBM}) increases by 3.3 (2.0) meV upon the adsorption of Mn_{12}.

Table I shows the distribution of excess charges at the interface of Mn_{12}|Gr|GaAs based on Mulliken charge analysis. The electron distribution for Mn_{12}|Gr|GaAs under zero doping level is subtracted as a reference. As seen from the table, the number of electrons on Mn_{12} barely changes except at $\rho = -1.00 \times 10^{13}\,\mathrm{cm}^{-2}$, where 0.06 ($\approx 0.61 \times 10^{-3} \times 100$) electrons are added to Mn_{12}. Graphene gains 0.56 ($\approx 1.67 \times 10^{-3} \times 338$) at a doping level of $\rho = -1.00 \times 10^{13}\,\mathrm{cm}^{-2}$, and it loses 0.06 ($\approx |-0.17| \times 10^{-3} \times 338$) electrons at a doping level of $+1.00 \times 10^{13}\,\mathrm{cm}^{-2}$. This is consistent with our previous observation that electron doping results in a larger shift of the Dirac point than hole doping. The first GaAs layer tends to lose (gain) electrons when graphene gains (loses) electrons. This is likely due to the Coulomb repulsion between these two adjacent atomic layers. The number of electrons gained by the first GaAs layer does not change monotonically with the hole-doping level, but reaches a maximum at $\rho = +0.10 \times 10^{13}\,\mathrm{cm}^{-2}$. This observation supports that GaAs is doped with holes at a doping level between $\rho = +0.10 \times 10^{13}\,\mathrm{cm}^{-2}$ and $\rho = +0.50 \times 10^{13}\,\mathrm{cm}^{-2}$.

Compared with zero doping, the Mn_8O_8 ring, the Mn_4O_4 core, the COOH groups, and the H_2O units of Mn_{12} gain 8.18×10^{-3}, 1.84×10^{-3}, 47.70×10^{-3}, and 3.59×10^{-3} electrons, respectively, at the charge-doping level of $\rho = -1.00 \times 10^{13}\,\mathrm{cm}^{-2}$. Although the COOH groups gain much more charge than the Mn_8O_8 ring in total, one Mn^{3+} ion (in the Mn_8O_8 ring) gains more electrons than one atom in the COOH groups on average (see Fig. 5). The average amount of electrons gained by one Mn^{3+} ion is about four times larger than that gained by one Mn^{4+} ion (in the Mn_4O_4 core). For both Mn^{3+} and Mn^{4+} ions, the spin-up channel gains and the spin-down channel loses electrons. Since the highest occupied spin-down molecular orbital is well below the Fermi level and thus remains fully occupied, the loss of electrons in the spin-down channel is due to the deformation of occupied states. According to Boukhvalov *et al.* [74], redistribution of electron density affects the magnetic exchange interactions between Mn atoms.

Let $V_{\mathrm{H}}(\rho, z)$ be the plane-averaged (over the $x-y$ plane) Hartree potential of Mn_{12}|Gr|GaAs at position z for charge doping density ρ. Figure 6 shows $\delta V_{\mathrm{H}} = V_{\mathrm{H}}(\rho, z) - V_{\mathrm{H}}(0, z)$,

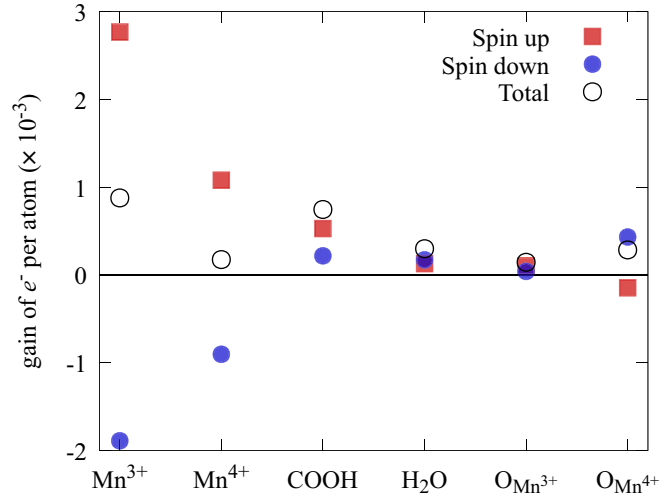

FIG. 5. Mulliken charge analysis for Mn_{12} within Mn_{12}|Gr|GaAs at a doping level of $\rho = -1.00 \times 10^{13}\,\mathrm{cm}^{-2}$. The charge distribution at zero doping is subtracted as a reference. $O_{Mn^{3+}}$ ($O_{Mn^{4+}}$) denotes oxygen atoms in the Mn_8O_8 ring (Mn_4O_4 center).

which can be viewed as the gate potential. We focus on three regions: (1) the region between GaAs and graphene, (2) the region between graphene and Mn_{12}, and (3) the region beyond Mn_{12}. Let regions i ($i = 1, 2$, and 3) begin at z_1^i and end at z_2^i. We define the gate potential buildup across region i to be $\Delta_i = \delta V_{\mathrm{H}}(z_2^i) - \delta V_{\mathrm{H}}(z_1^i)$, where the argument ρ is dropped for brevity. Within the charge density range $[-0.50 : 1.00] \times 10^{13}\,\mathrm{cm}^{-2}$, Δ_1 is effectively tuned, whereas Δ_2 is not. This is consistent with Fig. 4, in the sense that the band alignment between graphene and GaAs (Mn_{12}) is (is not) effectively tuned. Within the same charge density range, Δ_3

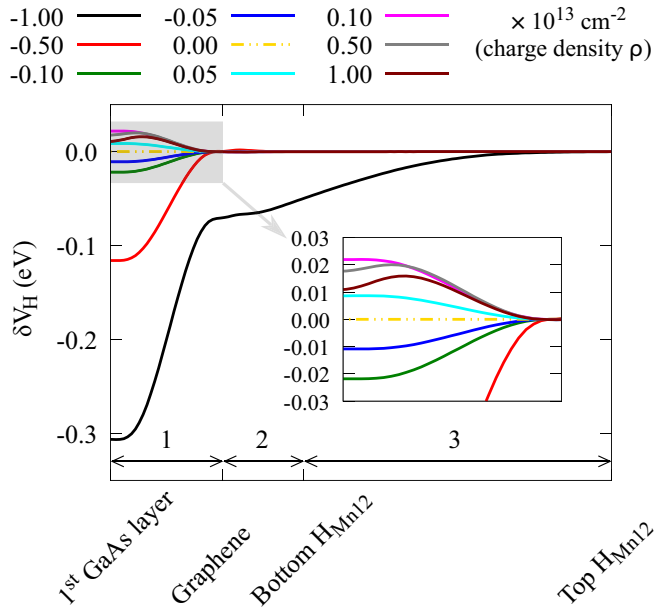

FIG. 6. Hartree potential difference $\delta V_{\mathrm{H}} = V_{\mathrm{H}}(\rho, z) - V_{\mathrm{H}}(0, z)$ of Mn_{12}|Gr|GaAs. The horizontal arrows indicate the three regions indexed by 1, 2, and 3. H_{Mn12} denotes a $-$H ligand of Mn_{12}. The inset zooms in on the region shaded in gray.

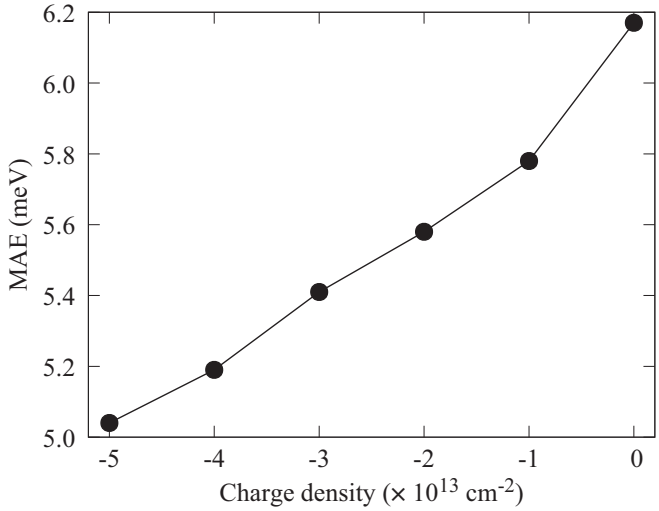

FIG. 7. Magnetic anisotropy energy (MAE) versus charge doping density for Mn_{12}|Gr.

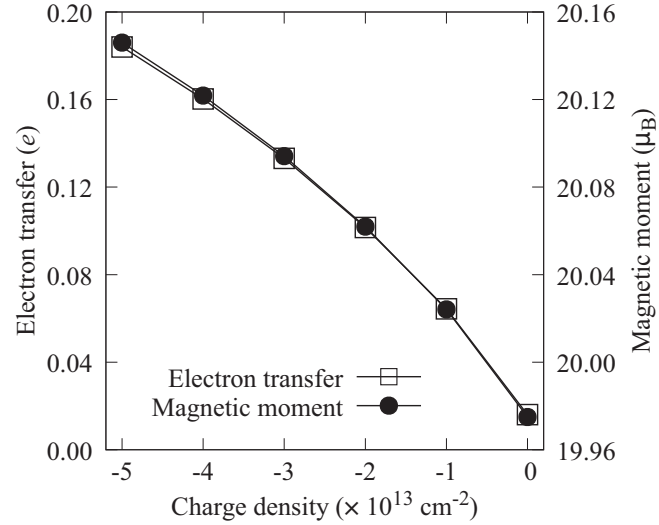

FIG. 8. Number of electrons transferred from graphene to Mn_{12} (left-hand scale) and magnetic moment of Mn_{12} (right-hand scale) versus electrostatic doping level. A negative charge density means electron doping.

remains almost zero, which signifies that the gate electric field does not extend across Mn_{12}. At $\rho = -1.00 \times 10^{13}\,\mathrm{cm}^{-2}$, both Δ_2 and Δ_3 are significantly tuned as a result of Mn_{12} being doped with electrons. The gate electric field $\mathcal{E}_i$ in region i is determined by $e\mathcal{E}_i = \Delta_i/(z_2^i - z_1^i)$, where e is the unit charge (a positive value). $\mathcal{E}_1$, $\mathcal{E}_2$, and $\mathcal{E}_3$ are 0.69, 0.08, and 0.05 V/nm, respectively, at $\rho = -1.00 \times 10^{13}\,\mathrm{cm}^{-2}$. Recall that GaAs becomes doped with holes at a doping level between $\rho = 0.10 \times 10^{13}\,\mathrm{cm}^{-2}$ and $\rho = 0.50 \times 10^{13}\,\mathrm{cm}^{-2}$. As a consequence, $\mathcal{E}_1 = -0.06\,\mathrm{V/nm}$ at $\rho = 0.10 \times 10^{13}\,\mathrm{cm}^{-2}$ is larger in magnitude than $\mathcal{E}_1 = -0.05\,\mathrm{V/nm}$ at $\rho = 0.50 \times 10^{13}\,\mathrm{cm}^{-2}$, although the doping level for the latter is higher. Note that the adsorption of Mn_{12} does not affect the Hartree potential between GaAs and graphene by much (less than 1 meV) within the charge density range $[-1.00 : 1.00] \times 10^{13}\,\mathrm{cm}^{-2}$. This implies that the electron tunneling rate between GaAs and graphene in transport measurements is similar with and without the presence of Mn_{12}.

C. Magnetic anisotropy

Next, we examine how electrostatic doping affects the MAE of Mn_{12}. We have shown in Sec. III B that electrons can be added to but cannot be taken from Mn_{12} at moderate doping levels. Therefore, we consider the effects of electron doping on MAE in particular. When the charge doping density is higher in magnitude than $-1.00 \times 10^{13}\,\mathrm{cm}^{-2}$, there are only graphene and Mn_{12} states near the Fermi level. According to second-order perturbation theory [75], the MAE is dominated by pairs of occupied and unoccupied states around the Fermi level. Therefore, it should be a good approximation to calculate MAE without GaAs. Based on the heterostructure Mn_{12}|Gr without GaAs, we calculate the MAE as $\mathrm{MAE} = E_\perp - E_\parallel$, where $E_\perp$ ($E_\parallel$) is the DFT total energy for the spin of Mn_{12} perpendicular (parallel) to the magnetic easy axis. The calculated MAE of Mn_{12}|Gr versus the charge doping density is shown in Fig. 7. As seen from the figure, the MAE decreases as the electron-doping level increases. The MAE at $\rho = -5.0 \times 10^{13}\,\mathrm{cm}^{-2}$ decreases by about 18% compared with the value at zero doping. It is noteworthy that the MAE of Mn_{12}|Gr at zero doping is 1% smaller than the MAE of an isolated Mn_{12} [4].

We can relate the decrease in MAE in terms of electron transfer from graphene to Mn_{12}. Figure 8 shows the number of electrons transferred from graphene to Mn_{12} versus the charge doping density. The number of electrons added to Mn_{12} increases with the electron doping density, and about 0.18 electrons are added to Mn_{12} at $\rho = -5.0 \times 10^{13}\,\mathrm{cm}^{-2}$. Along with the electron transfer, the magnetic moment of Mn_{12}, in units of Bohr magneton, increases by nearly the same amount as the number of electrons transferred. The magnetic moment of Mn_{12} increases rather than decreases since the spin polarization of the LUMO orbital, which receives the added electrons, is parallel to the total spin of the whole Mn_{12} molecule. Previously, Park and Pederson considered potassium addition to introduce extra electrons on Mn_{12} [6]. They found that the MAE of Mn_{12} decreases by 15%, 37%, and 56% with one, two, and four extra electrons, respectively. As a numerical experiment, we add extra electrons to a single isolated Mn_{12} molecule which has the same atomic positions as the Mn_{12} molecule of the Mn_{12}|Gr heterostructure. The MAE of the isolated Mn_{12} molecule decreases as the number of added electrons increases from zero to one. The MAE of isolated Mn_{12} decreases by 15% with one additional electron, coincident with Park and Pederson's findings. This confirms that electron transfer from graphene to Mn_{12} is responsible for the decrease in the MAE of Mn_{12}|Gr under electron doping.

However, with 0.18 additional electrons, the MAE of isolated Mn_{12} decreases by 2%, which is much smaller than the decrease of 18% in the MAE of Mn_{12}|Gr. This can be understood within second-order perturbation theory, where pairs of occupied and unoccupied states can be classified into three types, Mn_{12}-Mn_{12}, graphene-graphene, and Mn_{12}-graphene. The 2% decrease in the MAE of the isolated Mn_{12} can be understood as a decrease in the

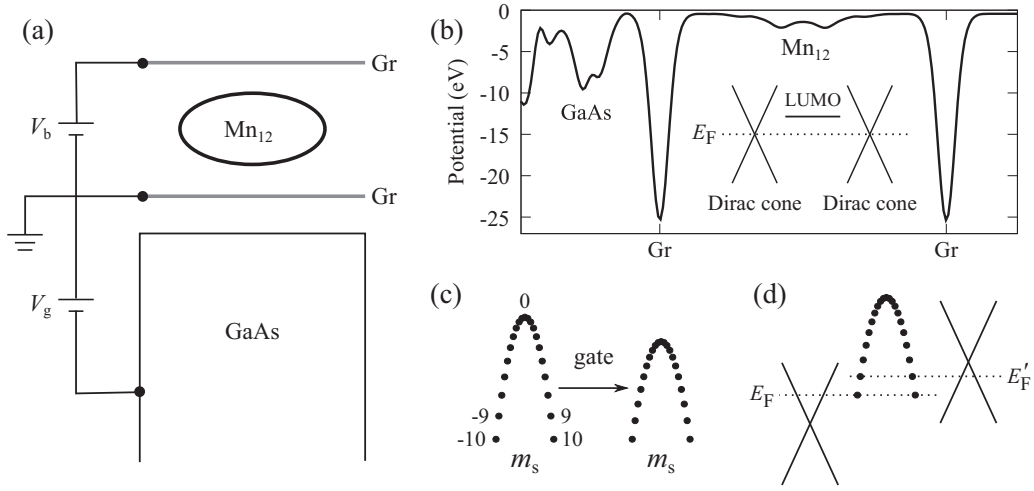

FIG. 9. (a) Illustration of a Gr|Mn_{12}|Gr|GaAs tunnel junction. V_g is gate voltage, and V_b is bias voltage. The two graphene layers are separated by about 1.42 nm. (b) Calculated plane-averaged electrostatic potential of the junction. The inset shows schematic band alignment between the Mn_{12} molecule and the two graphene layers. (c) Spin excitations with zero gate and with a finite gate. $|m_s\rangle$ are spin states with $m_s = \pm 10, \pm 9, \ldots, 0$. (d) Band alignment when a spin excitation enters the bias window.

contribution from the Mn_{12}-Mn_{12} pairs. Since contributions to the MAE from graphene-graphene pairs are negligibly small (as seen from isolated graphene), we owe the extra reduction in the MAE of Mn_{12}|Gr to a decrease in the contribution from the Mn_{12}-graphene pairs. Such an argument is supported by the observation that electron doping dramatically changes the band alignment between Mn_{12} and graphene and thus the pairs of occupied graphene (Mn_{12}) states and unoccupied Mn_{12} (graphene) states around the Fermi level. Note that the change in the band alignment between Mn_{12} and graphene is mainly caused by electrostatic doping rather than by electron transfer between Mn_{12} and graphene. Thus, the change in the band alignment between Mn_{12} and graphene is another factor that is responsible for the decrease in the MAE of Mn_{12}|Gr under electron doping.

To investigate the possible role of a local electric field between Mn_{12} and graphene, we take the isolated Mn_{12} molecule again and move it close to (2.46 Å away from) the plane where the boundary condition of constant electrostatic potential is enforced. In this way, we retain a strong local electric field below Mn_{12} when the Mn_{12} molecule is charged. Otherwise, the local electric field is not as strong in our earlier numerical experiment using the isolated Mn_{12} molecule. It turns out that the decrease in MAE is still 2% with 0.18 additional electrons even though a strong local electric field is present below Mn_{12}. Therefore, we exclude the local electric field between Mn_{12} and graphene and the associated electric field across Mn_{12} as a separate reason for the decrease in the MAE of Mn_{12}|Gr under electron doping. From perturbation theory [76], magnetic anisotropy of molecules is closely related to a molecular quadrupole moment, which should change with gate electric field. Since we determine molecular orbitals and thus electron density self-consistently, the change in molecular quadrupole moment and its influence on MAE have been captured implicitly by our calculations. However, the effect of electric field on MAE via spin-orbit coupling amplitude is still unknown.

D. A vertical tunnel junction

In this section, we propose a vertical tunnel junction for detecting the gate dependence of MAE discussed in the previous section. The junction is illustrated in Fig. 9(a), where a Mn_{12} molecule is sandwiched between two graphene layers. The bottom graphene layer should be supported by *n*-type GaAs, which has conducting charge carriers at low temperature (several Kelvins) [44,45]. A gate voltage V_g is applied between the bottom graphene layer and the GaAs and a bias

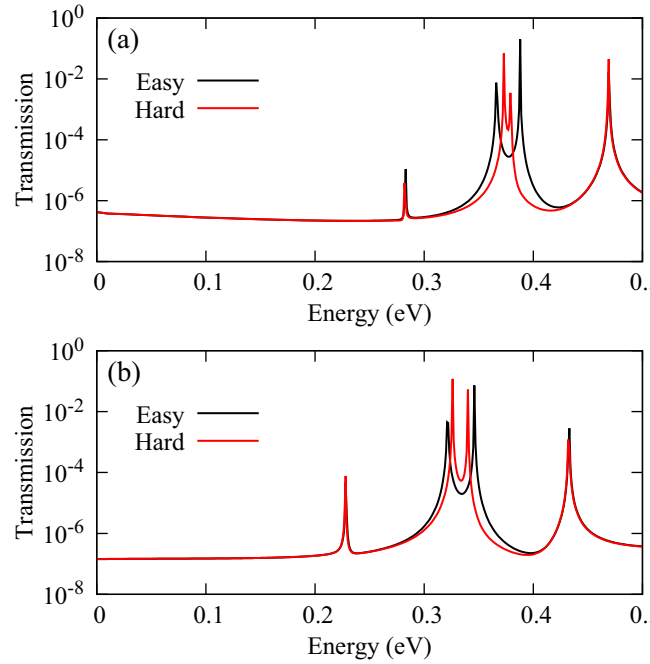

FIG. 10. Electron transmission of a Gr|Mn_{12}|Gr junction under (a) zero doping and (b) an electron doping level of $\rho = -5 \times 10^{13}$ cm^{-2}. The black (red) line is for the spin aligned in the easy (a hard) direction. The Fermi level is set to zero.

voltage V_b between the bottom and top graphene layers. In the proposed vertical tunnel junction, GaAs is electron doped to bring the conduction band near the Fermi level. Such a band alignment may change the behavior of the system substantially compared to the results presented in previous sections. Assuming a similar response of MAE to a gate electric field, we argue that the gate dependence of MAE can be probed by measuring the electron tunneling current I through Mn_{12} as a function of V_g and V_b.

First, we construct an atomic structure of the tunnel junction by adding a flat graphene layer above the Mn_{12}|Gr|GaAs heterostructure, and calculate from first principles the electronic structure of the junction at zero gate and zero bias. Figure 9(b) shows the plane-averaged electrostatic potential (Hartree potential and ionic potential) across the tunnel junction. The electrostatic potential around the bottom graphene layer is similar to that around the top graphene layer. The inset of Fig. 9(b) depicts a schematic band alignment of the junction. According to our calculations, the Dirac points of either graphene layer are at the Fermi level and the LUMO of Mn_{12} is 0.230 eV above the Fermi level. To estimate the structural change in Mn_{12} caused by a finite bias voltage, we apply static electric fields on a single isolated Mn_{12} molecule. At 0.2 V/Å (≈2.84 V across the junction), the maximal change in Mn–O bonds is 0.032 Å and the change in all other chemical bonds is below 0.003 Å. At 0.1 V/Å, the change in all bond lengths is within 0.018 Å. Because the S_z degeneracy is broken by the spin-orbit interaction, below the LUMO energy there should be spin states of Mn_{12} on an energy scale of 1 meV relative to the ground-state energy of Mn_{12}. Such spin states are detectable via transport measurements in single-molecule break junctions based on previous studies [77–79].

The mechanism for detecting spin excitations in a tunneling current is similar to the approach for magnetic tunnel junctions [80,81]. The spin excitations can also be probed in the vertical tunnel junction shown in Fig. 9(a). As established in Sec. III C, the MAE of Mn_{12} can be reduced by electron doping. Consequently, the energy spacings between spin excitations are reduced, as illustrated in Fig. 9(c). This is likely the case even though Mn_{12} is fractionally charged and the spin projection m_s is no longer a good quantum index. At finite bias voltages, the Fermi level of the bottom graphene layer E_F is different from that of the top graphene E_F'. We call the energy range between E_F and E_F' the bias window. Whenever a spin excitation enters the bias window [see an illustration in Fig. 9(d)], an additional transmission path through the excitation of the spin state is opened, leading to a sudden increase in the tunneling current I. The record of multiple spin excitations allows determination of the energy spacings between these spin excitations, and thus the MAE of Mn_{12}. As gate voltage varies, the gate dependence of MAE can then be probed.

In general, one can expect a sensitive change of the tunneling current due to the spin state of the SMM in the junction. Therefore, tunneling measurements can be used as a more general probe of the spin state of the SMM than just the MAE. We comment that the usual DFT plus nonequilibrium Green's function (DFT + NEGF) approach [82] cannot capture the transport signals due to spin excitations. See Appendix C for DFT + NEGF results at zero bias voltage.

IV. CONCLUSION AND DISCUSSION

In conclusion, we have simulated gate field effects on the heterostructures Mn_{12}|Gr|GaAs, Gr|GaAs, and Mn_{12}|Gr. In the Mn_{12}|Gr|GaAs heterostructure, Mn_{12} can gain but not lose electrons at moderate doping levels. The MAE of Mn_{12} adsorbed on graphene decreases by about 18% at an electron-doping level of -5.00×10^{13} cm^{-2}. Such a decrease in the MAE is due to electron transfer from graphene to Mn_{12} as well as the change in the band alignment between Mn_{12} and graphene. The band alignment between graphene and GaAs is more sensitive to electron doping than to hole doping. At an electron-doping level of -1.00×10^{13} cm^{-2}, the Dirac point of graphene is lifted by about 0.24 eV relative to the VBM of GaAs. Compared with electrostatic doping, the adsorption of Mn_{12} does not have much effect on the band alignment between graphene and GaAs. The GaAs substrate induces a band gap of about 2.2 meV in graphene due to the interaction between GaAs and graphene. It remains to study gate field effects on similar heterostructures with other ligands around the $Mn_{12}O_{12}(COOR)_{16}(H_2O)_4$ molecule.

ACKNOWLEDGMENTS

This work was supported by the Center for Molecular Magnetic Quantum Materials, an Energy Frontier Research Center funded by the U.S. Department of Energy, Office of Science, Basic Energy Sciences under Award No. DE-SC0019330. Computations were done using the utilities of the National Energy Research Scientific Computing Center and the University of Florida Research Computing.

APPENDIX A: BASIS SET IN SIESTA CALCULATIONS

Our input specifications for the basis set in SIESTA are given in Table II. For an accurate description of magnetic properties, we applied DZP basis functions for Mn and O atoms. The remaining atoms (C, H, Ga, and As) employ SZP

TABLE II. Specifications of basis set. n and l are respectively the principal quantum number and angular momentum of the shell. $rc_{(1/2)}$ is the cutoff radius of the first/second basis function for this shell. rc_2 is not available (NA) for single-ζ basis set.

Element	n	l	rc_1 (Bohr)	rc_2 (Bohr)	Polarization functions
Mn	4	0	6.44	4.84	Y
Mn	3	2	4.84	2.83	N
O	2	0	4.30	2.95	N
O	2	1	4.91	3.35	Y
H	1	0	5.20	NA	Y
C of Mn_{12}	2	0	4.89	NA	N
C of Mn_{12}	2	1	5.84	NA	Y
C of Gr	2	0	4.71	NA	N
C of Gr	2	1	5.74	NA	Y
Ga	3	2	5.00	NA	N
Ga	4	0	5.98	NA	N
Ga	4	1	8.45	NA	Y
As	4	0	5.06	NA	N
As	4	1	5.27	NA	Y
H.75	1	0	5.52	NA	Y

TABLE III. Convergence test on Mn_{12}|Gr with respect to the smearing temperature T. The k-point grid is fixed at 6×6. N_e is the number of electrons on Mn_{12} (Mulliken charge). M is total magnetic moment. E_{Dirac} is the position (in energy) of the Dirac point relative to the Fermi energy.

T (K)	N_e	M (μ_B)	E_{Dirac} (meV)
400	460.036436	19.9992	0.1
300	460.036438	19.9989	0.1
200	460.036437	19.9983	0.1
100	460.036434	19.9964	0.1
50	460.036437	19.9918	0.1

basis functions. The basis set for C atoms of Mn_{12} is different from those for graphene due to the different chemical environment, and the two basis sets are optimized for Mn_{12} and graphene separately.

APPENDIX B: CONVERGENCE TESTS

Table III shows test results on Mn_{12}|Gr for different smearing temperatures. When the smearing temperature is reduced from 400 K to 50 K, the number of electrons on Mn_{12} (Mulliken charge) varies by less than 1×10^{-5}, the total magnetic moment of the hetero-structure varies by less than 0.01 μ_B, and the position (in energy) of the Dirac point varies by less than 0.1 meV. This indicates that a smearing temperature of 200 K yields reliable electronic and magnetic properties. Table IV shows test results on Mn_{12}|Gr for different k-point grids. All k-point grids contain the K point where the Dirac point lies, and they yield the same energy of the Dirac point.

TABLE IV. Convergence test on Mn_{12}|Gr with respect to the k-point grid. The smearing temperature T is fixed at 200 K. The quantities are the same with those in Table III.

k-grid	N_e	M (μ_B)	E_{Dirac} (meV)
3×3	460.036385	19.9917	0.1
6×6	460.036437	19.9983	0.1
9×9	460.036448	19.9994	0.1
12×12	460.036450	19.9997	0.1

The variation in both the number of electrons and the total magnetic moment are insignificant when the k-point grid is denser than 3×3. These test results support that a 6×6 k-point grid yields reliable electronic and magnetic properties.

APPENDIX C: ELECTRON TRANSMISSION

We calculated electron transmission for a Gr|Mn_{12}|Gr junction under zero bias by Caroli's formula [83]. The Green's functions in Caroli's formula are based on the Kohn-Sham Hamiltonian with spin-orbit coupling. Due to the huge system size (1148 atoms), we included only the Γ point for both SCF and transport calculations. Figure 10 shows the electron transmission as a function of energy above the Fermi level (set at zero). There are four peaks, corresponding to the LUMO (at 0.2 eV), LUMO + 1, LUMO + 2, and LUMO + 3 orbitals, respectively. There are no peaks due to spin excitations, which are a few meV above the Fermi level in Fig. 10. It requires theoretical development beyond the DFT + NEGF method to obtain electron transport signals due to spin excitations. It is noteworthy that both absolute and relative peak positions are tunable by electron doping as well as by spin alignment.

[1] R. Sessoli, H. L. Tsai, A. R. Schake, S. Y. Wang, J. B. Vincent, K. Folting, D. Gatteschi, G. Christou, and D. N. Hendrickson, J. Am. Chem. Soc. **115**, 1804 (1993).

[2] A. L. Barra, D. Gatteschi, and R. Sessoli, Phys. Rev. B **56**, 8192 (1997).

[3] M. R. Pederson and S. N. Khanna, Phys. Rev. B **59**, R693 (1999).

[4] X. G. Li, J. N. Fry, and H. P. Cheng, Phys. Rev. B **90**, 125447 (2014).

[5] L. Michalak, C. M. Canali, M. R. Pederson, M. Paulsson, and V. G. Benza, Phys. Rev. Lett. **104**, 017202 (2010).

[6] K. Park and M. R. Pederson, Phys. Rev. B **70**, 054414 (2004).

[7] S. Hill, Polyhedron **64**, 128 (2013).

[8] P. Artus, C. Boskovic, J. Yoo, W. E. Streib, L. C. Brunel, D. N. Hendrickson, and G. Christou, Inorg. Chem. **40**, 4199 (2001).

[9] A. L. Barra, A. Caneschi, A. Cornia, D. Gatteschi, L. Gorini, L. P. Heiniger, R. Sessoli, and L. Sorace, J. Am. Chem. Soc. **129**, 10754 (2007).

[10] G. Q. Bian, T. Kuroda-Sowa, N. Gunjima, M. Maekawa, and M. Munakata, Inorg. Chem. Commun. **8**, 208 (2005).

[11] G. Q. Bian, T. Kuroda-Sowa, H. Konaka, M. Hatano, M. Maekawa, M. Munakata, H. Miyasaka, and M. Yamashita, Inorg. Chem. **43**, 4790 (2004).

[12] N. E. Chakov, S. C. Lee, A. G. Harter, P. L. Kuhns, A. P. Reyes, S. O. Hill, N. S. Dalal, W. Wernsdorfer, K. A. Abboud, and G. Christou, J. Am. Chem. Soc. **128**, 6975 (2006).

[13] N. E. Chakov, M. Soler, W. Wernsdorfer, K. A. Abboud, and G. Christou, Inorg. Chem. **44**, 5304 (2005).

[14] N. E. Chakov, W. Wernsdorfer, K. A. Abboud, D. N. Hendrickson, and G. Christou, Dalton Trans. **2003**, 2243 (2003).

[15] N. E. Chakov, L. N. Zakharov, A. L. Rheingold, K. A. Abboud, and G. Christou, Inorg. Chem. **44**, 4555 (2005).

[16] M. Fonin, S. Voss, S. Herr, G. de Loubens, A. D. Kent, M. Burgert, U. Groth, and U. Rudiger, Polyhedron **28**, 1977 (2009).

[17] S. M. George, S. I. Mamun, and J. Kim, Inorg. Chem. Commun. **13**, 429 (2010).

[18] N. Hoshino, T. Shiga, H. Oshio, and T. Akutagawa, Dalton Trans. **42**, 4377 (2013).

[19] T. Kuroda-Sowa, T. Nogami, H. Konaka, M. Maekawa, M. Munakata, H. Miyasaka, and M. Yamashita, Polyhedron **22**, 1795 (2003).

[20] L. A. Kushch, V. D. Sasnovskaya, A. I. Dmitriev, E. B. Yagubskii, O. V. Koplak, L. V. Zorina, and D. W. Boukhvalov, Dalton Trans. **41**, 13747 (2012).

[21] C. Lampropoulos, M. Murugesu, A. G. Harter, W. Wernsdofer, S. Hill, N. S. Dalal, A. P. Reyes, P. L. Kuhns, K. A. Abboud, and G. Christou, Inorg. Chem. **52**, 258 (2013).
[22] C. Lampropoulos, G. Redler, S. Data, K. A. Abboud, S. Hill, and G. Christou, Inorg. Chem. **49**, 1325 (2010).
[23] J. M. Lim, Y. Do, and J. Kim, Eur. J. Inorg. Chem. **2006**, 711 (2006).
[24] D. Ruiz-Molina, P. Gerbier, E. Rumberger, D. B. Amabilino, I. A. Guzei, K. Folting, J. C. Huffman, A. Rheingold, G. Christou, J. Veciana, and D. N. Hendrickson, J. Mater. Chem. **12**, 1152 (2002).
[25] M. Soler, P. Artus, K. Folting, J. C. Huffman, D. N. Hendrickson, and G. Christou, Inorg. Chem. **40**, 4902 (2001).
[26] H. L. Tsai, D. M. Chen, C. I. Yang, T. Y. Jwo, C. S. Wur, G. H. Lee, and Y. Wang, Inorg. Chem. Commun. **4**, 511 (2001).
[27] H. L. Tsai, H. A. Shiao, T. Y. Jwo, C. I. Yang, C. S. Wur, and G. H. Lee, Polyhedron **24**, 2205 (2005).
[28] S. Verma, A. Verma, A. K. Srivastava, A. Gupta, S. P. Singh, and P. Singh, Mater. Chem. Phys. **177**, 140 (2016).
[29] S. W. Yoon, M. Heu, W. S. Jeon, D. Y. Jung, B. J. Suh, and S. Yoon, Phys. Rev. B **67**, 052402 (2003).
[30] V. S. Zagaynova, T. L. Makarova, N. G. Spitsina, and D. W. Boukhvalov, J. Supercond. Novel Magn. **24**, 855 (2011).
[31] H. H. Zhao, C. P. Berlinguette, J. Bacsa, A. V. Prosvirin, J. K. Bera, S. E. Tichy, E. J. Schelter, and K. R. Dunbar, Inorg. Chem. **43**, 1359 (2004).
[32] L. Zobbi, M. Mannini, M. Pacchioni, G. Chastanet, D. Bonacchi, C. Zanardi, R. Biagi, U. Del Pennino, D. Gatteschi, A. Cornia, and R. Sessoli, Chem. Commun. **2005**, 1640 (2005).
[33] S. M. J. Aubin, Z. M. Sun, L. Pardi, J. Krzystek, K. Folting, L. C. Brunel, A. L. Rheingold, G. Christou, and D. N. Hendrickson, Inorg. Chem. **38**, 5329 (1999).
[34] H. J. Eppley, H. L. Tsai, N. Devries, K. Folting, G. Christou, and D. N. Hendrickson, J. Am. Chem. Soc. **117**, 301 (1995).
[35] M. Soler, S. K. Chandra, D. Ruiz, E. R. Davidson, D. N. Hendrickson, and G. Christou, Chem. Commun. **2000**, 2417 (2000).
[36] H.-L. Tsai, T.-Y. Jwo, G.-H. Lee, and Y. Wang, Chem. Lett. **29**, 346 (2000).
[37] E. Coronado, A. Forment-Aliaga, A. Gaita-Arino, C. Gimenez-Saiz, F. M. Romero, and W. Wernsdorfer, Angew. Chem. Int. Ed. **43**, 6152 (2004).
[38] F. Rostamzadeh Renani and G. Kirczenow, Phys. Rev. B **85**, 245415 (2012).
[39] J. Hu and R. Q. Wu, Phys. Rev. Lett. **110**, 097202 (2013).
[40] N. Tsukahara, K. I. Noto, M. Ohara, S. Shiraki, N. Takagi, Y. Takata, J. Miyawaki, M. Taguchi, A. Chainani, S. Shin, and M. Kawai, Phys. Rev. Lett. **102**, 167203 (2009).
[41] Y. C. Zhang, J. Chem. Phys. **146**, 194705 (2017).
[42] S. Barraza-Lopez, M. C. Avery, and K. Park, Phys. Rev. B **76**, 224413 (2007).
[43] X. C. Zhu, A. Hale, G. Christou, and A. F. Hebard, J. Appl. Phys. **127**, 064303 (2020).
[44] J. S. Blakemore, J. Appl. Phys. **53**, R123 (1982).
[45] S. Tongay, A. F. Hebard, Y. Hikita, and H. Y. Hwang, Phys. Rev. B **80**, 205324 (2009).
[46] R. Z. Bachrach, R. S. Bauer, P. Chiaradia, and G. V. Hansson, J. Vac. Sci. Technol. **18**, 797 (1981).
[47] D. K. Biegelsen, R. D. Bringans, J. E. Northrup, and L. E. Swartz, Phys. Rev. B **41**, 5701 (1990).
[48] D. K. Biegelsen, R. D. Bringans, J. E. Northrup, and L. E. Swartz, Phys. Rev. Lett. **65**, 452 (1990).
[49] A. Ohtake, J. Nakamura, T. Komura, T. Hanada, T. Yao, H. Kuramochi, and M. Ozeki, Phys. Rev. B **64**, 045318 (2001).
[50] A. M. Munshi, D. L. Dheeraj, V. T. Fauske, D. C. Kim, A. T. J. van Helvoort, B. O. Fimland, and H. Weman, Nano Lett. **12**, 4570 (2012).
[51] Q. L. Liu, Z. Y. Zhao, and J. H. Yi, J. Alloys Compd. **795**, 351 (2019).
[52] P. Hohenberg and W. Kohn, Phys. Rev. **136**, B864 (1964).
[53] W. Kohn and L. J. Sham, Phys. Rev. **140**, A1133 (1965).
[54] G. Kresse, J. Non-Cryst. Solids **193**, 222 (1995).
[55] G. Kresse and D. Joubert, Phys. Rev. B **59**, 1758 (1999).
[56] J. M. Soler, E. Artacho, J. D. Gale, A. Garcia, J. Junquera, P. Ordejon, and D. Sanchez-Portal, J. Phys.: Condens. Matter **14**, 2745 (2002).
[57] P. E. Blochl, Phys. Rev. B **50**, 17953 (1994).
[58] J. Klimes, D. R. Bowler, and A. Michaelides, Phys. Rev. B **83**, 195131 (2011).
[59] J. P. Perdew, K. Burke, and M. Ernzerhof, Phys. Rev. Lett. **77**, 3865 (1996).
[60] N. Troullier and J. L. Martins, Phys. Rev. B **43**, 1993 (1991).
[61] J. D. Pack and H. J. Monkhorst, Phys. Rev. B **16**, 1748 (1977).
[62] M. Methfessel and A. T. Paxton, Phys. Rev. B **40**, 3616 (1989).
[63] M. Otani and O. Sugino, Phys. Rev. B **73**, 115407 (2006).
[64] L. G. Ferreira, M. Marques, and L. K. Teles, Phys. Rev. B **78**, 125116 (2008).
[65] J. H. Yuan, Q. Chen, L. R. C. Fonseca, M. Xu, K. H. Xue, and X. S. Miao, J. Phys. Commun. **2**, 105005 (2018).
[66] M. Ribeiro, L. R. C. Fonseca, and L. G. Ferreira, Europhys. Lett. **94**, 27001 (2011).
[67] S. L. Dudarev, G. A. Botton, S. Y. Savrasov, C. J. Humphreys, and A. P. Sutton, Phys. Rev. B **57**, 1505 (1998).
[68] D. W. Boukhvalov, M. Al-Saqer, E. Z. Kurmaev, A. Moewes, V. R. Galakhov, L. D. Finkelstein, S. Chiuzbaian, M. Neumann, V. V. Dobrovitski, M. I. Katsnelson, A. I. Lichtenstein, B. N. Harmon, K. Endo, J. M. North, and N. S. Dalal, Phys. Rev. B **75**, 014419 (2007).
[69] G. B. Bachelet and M. Schlüter, Phys. Rev. B **25**, 2103 (1982).
[70] L. Kleinman, Phys. Rev. B **21**, 2630 (1980).
[71] L. Fernández-Seivane, M. A. Oliveira, S. Sanvito, and J. Ferrer, J. Phys.: Condens. Matter **18**, 7999 (2006).
[72] R. Sessoli, D. Gatteschi, A. Caneschi, and M. A. Novak, Nature (London) **365**, 141 (1993).
[73] S. Voss, M. Burgert, M. Fonin, U. Groth, and U. Rudiger, Dalton Trans, 499 (2008).
[74] D. W. Boukhvalov, V. V. Dobrovitski, P. Kogerler, M. Al-Saqer, M. I. Katsnelson, A. I. Lichtenstein, and B. N. Harmon, Inorg. Chem. **49**, 10902 (2010).
[75] D. S. Wang, R. Q. Wu, and A. J. Freeman, Phys. Rev. B **47**, 14932 (1993).
[76] M. P. Brereton, M. K. Cooper, G. R. Dennis, and G. L. D. Ritchie, Aust. J. Chem. **34**, 2253 (1981).
[77] H. B. Heersche, Z. de Groot, J. A. Folk, H. S. J. van der Zant, C. Romeike, M. R. Wegewijs, L. Zobbi, D. Barreca,

E. Tondello, and A. Cornia, Phys. Rev. Lett. **96**, 206801 (2006).

[78] M. H. Jo, J. E. Grose, K. Baheti, M. M. Deshmukh, J. J. Sokol, E. M. Rumberger, D. N. Hendrickson, J. R. Long, H. Park, and D. C. Ralph, Nano Lett. **6**, 2014 (2006).

[79] A. S. Zyazin, J. W. G. van den Berg, E. A. Osorio, H. S. J. van der Zant, N. P. Konstantinidis, M. Leijnse, M. R. Wegewijs, F. May, W. Hofstetter, C. Danieli, and A. Cornia, Nano Lett. **10**, 3307 (2010).

[80] S. Zhang, P. M. Levy, A. C. Marley, and S. S. P. Parkin, Phys. Rev. Lett. **79**, 3744 (1997).

[81] G. X. Du, S. G. Wang, Q. L. Ma, Y. Wang, R. C. C. Ward, X.-G. Zhang, C. Wang, A. Kohn, and X. F. Han, Phys. Rev. B **81**, 064438 (2010).

[82] J. Taylor, H. Guo, and J. Wang, Phys. Rev. B **63**, 121104(R) (2001).

[83] C. Caroli, R. Combescot, P. Nozieres, and D. Saint-James, J. Phys. C **4**, 916 (1971).